Research Article

A 1-D Convolutional Neural Network with Gradient Mapped Intensity Features for Detection of Mitosis in Histopathological Images

Akarsh Jagadeesha* and Devaraj Verma C.
Department of CSE, FET, Jain (Deemed-to-be) University, Bengaluru, Karnataka, India

Panita Wannapiroon
Information and Communication Technology for Education, Technical Education, King Mongkut's University of Technology North Bangkok, Bangkok, Thailand

Junjiraporn Thongprasit
Academic Enhancement Department, King Mongkut's University of Technology North Bangkok, Bangkok, Thailand

* Corresponding author. E-mail: j.akarsh@jainuniversity.ac.in DOI: 10.14416/j.asep.2025.07.010
Received: 25 March 2025; Revised: 30 June 2025; Accepted: 15 July 2025; Published online: 23 July 2025

Abstract
This paper proposes a mitosis detection algorithm that utilizes gradient-mapped intensity (GMI) features integrated into a one-dimensional convolutional neural network (1-D CNN) for the classification of mitotic cells in histopathological images. The proposed framework begins by preprocessing the input images through intensity compensation, followed by contrast enhancement using adaptive histogram equalization. Mitosis candidates are subsequently identified using adaptive thresholding techniques and morphological operations. From each detected candidate, GMI features are extracted through gradient estimation in both the x and y directions, construction of gradient histograms, and mapping of gradient magnitudes with corresponding intensity values. These features, derived from the red, green, and blue (RGB) channels, are used to train a 1-D CNN classifier that categorizes the inputs into two classes: mitosis and non-mitosis. The effectiveness of the proposed approach is evaluated using two benchmark datasets, ICPR 2012 and ICPR 2014, with performance measured via precision, recall, and F1-score metrics. The proposed model achieves an F1-score of 0.846, a recall of 0.859, and a precision of 0.863 on the ICPR 2012 dataset, demonstrating competitive performance compared to existing methods.

Keywords: 1-D convolution neural network (1-D CNN), F1-score, Gradient-mapped intensity (GMI), Histopathological image, Mitosis

1 Introduction

Due to the increase in the number of patients with breast cancer, the diagnosis of mitosis in tumor cells has become very essential [1]. It is a time-consuming and tedious task to perform a manual mitotic count. Hence, the automatic detection of mitotic tumor cells is required to complete the mitotic counting process in a short time without the need for high material resources and manpower. The mitosis process occurs in 4 stages, namely the prophase, followed by metaphase, anaphase, and telophase. There will be a high change in texture, morphology, color, and size of the cells in each stage. A few examples of mitosis and non-mitosis cells are illustrated in Figure 1.

The recent algorithms for the detection of mitosis can be broadly classified into three groups, namely object detection approach, semantic segmentation approach, and pixel classification approach. In the object detection approach [2], the training network

requires a bounding box along with its corresponding labels. In the semantic segmentation approach, the segmentation map is determined from the semantic segmentation [3]. Each pixel is categorized into two labels, which are the mitotic pixels, and non-mitotic pixels, where the network is trained using the categorized pixels. In the pixel classification approach, the pixels that are close to the centroid of the mitosis cell are considered mitosis cells, and the pixels that are away from the centroid are considered non-mitosis cells. Based on the consideration, the network is trained where a fixed patch for every pixel is provided to the training network. However, this approach has high computational and storage costs [4].

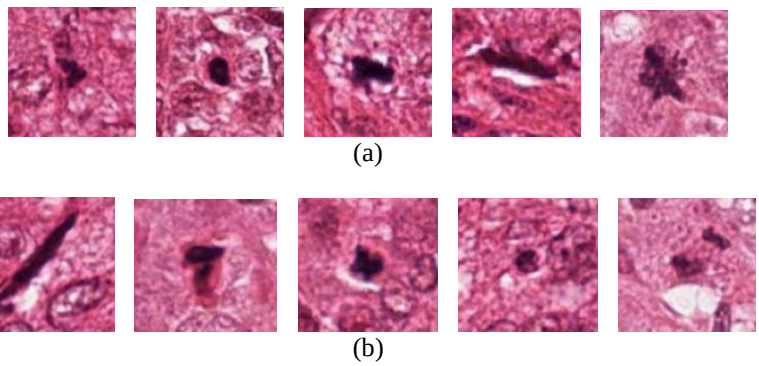

(a) (b)

Figure 1: Few examples of mitosis and non-mitosis cells (a) Mitosis cell (b) non-mitosis cell [5].

Deep learning algorithms play a major role in the detection of mitosis. The traditional CNN-based approach has the challenge that it requires a pixel-wise label to attain better performance. To provide pixel-wise labels, the pathologist needs to spend an enormous time. It is very challenging to apply the trained mitotic mode globally due to the staining procedures and variations caused due to various microscopic scanners. Li *et al*., [6] proposed a segmentation network based on the supervised instance and domain adaptive box. This approach minimizes the performance variations between the images collected from different scan equipment. Inoue *et al*., [7] proposed a fine-tuning algorithm for the supervised adaptation framework in two stages. The consistency between the adaption components was improved by Chen *et al*., [8], which uses a faster R-CNN network [9]. The compressed sensing approach was combined with a convolutional neural network [10] to perform the cell detection process. This approach reduces the inter-class imbalance by considering the classification problem as a regression problem. The refining of the label was performed by Sahail *et al*., [11]. However, refining the label reduces the performance of the images collected from other scanning equipment. To minimize such performance variations diverse training approach was proposed by Tellez *et al*., [12]. This improves the performance of the algorithm when working in different staining protocols by using the staining augmentation approach. Zhang *et al*., [13] used inter-domain consistency features that use adversarial learning. This approach ignores the irrelevant features while training the model. Lei [5] used a deep CNN to identify the mitosis candidate. The CNN features are reencoded using the spatial attention network. This spatial attention network enables the model to consider the more efficient features. The mitosis is selected from the mitosis candidate using a subnet formed by multi-branch classification.

Huang *et al*., [14] used the color information for the detection of mitosis using exclusive independent component analysis. Content-aware post-processing and Gamma Gaussian mixture model are used by the author Khan *et al*., [15] which reduces the negative samples. However, this approach has the drawback that the performance changes when tested on the histopathological images collected from different instruments. The authors Ciresan *et al*., [16] proposed a sliding window approach for the CNN classifier that learns the images by patches. A cascaded network was proposed by Chen *et al*., [17] that uses two different networks, namely the discriminant network and a rough search network. The rough search network initially detects the mitosis candidates, while the discriminant network selects the mitosis cells from the candidates. Wang *et al*., [18] used CNN to train the handcrafted features for mitosis detection. This approach is simple, however, the performance is reduced due to the usage of redundant features in

training the CNN. Faster- RCNN algorithms are also used in the detection [19] of mitosis where the algorithm proposed by Ren *et al*., [19] uses two stages, which are the candidate detection stage and fine-tuning stage. The coordinate information of the candidate is used in the fine-tuning stage to identify the mitosis cells. Squeeze and excitation block was proposed by Hu *et al*., [20], which adds the features of the channel domain with the weighting operations. The contribution of the paper is as follows. This paper proposes a mitosis detection algorithm from the mitosis candidates detected from the histopathological images. The algorithm extracts the gradient-mapped intensity features from the red, green, and blue channels, which highly differentiate the mitosis and non-mitosis candidates. The GMI process extracts and merges histogram and intensity features from the mitotic image, which results in a 1-D feature sequence. The algorithm also uses a 1-D-CNN [21] classifier that trains or classifies the mitosis candidates. Finally, the evaluation of the algorithm was done using the ICPR-2012 and ICPR-2014 datasets using the metrics called precision, F1-score, and recall. The algorithm designed can very well be extended for other mitosis detection datasets, cancer types and other cellular objects as well. Thereby, making it a worthy candidate for any classification problems when working with a histopathological image dataset.

2 Materials and Methods

The block diagram of the proposed mitosis detection algorithm is illustrated in Figure 2. The proposed mitosis detection algorithm includes four processes including pre-processing, segmentation of mitosis candidate, extraction of gradient mapped intensity (GMI) feature, and training/classification of candidate feature using 1-D CNN.

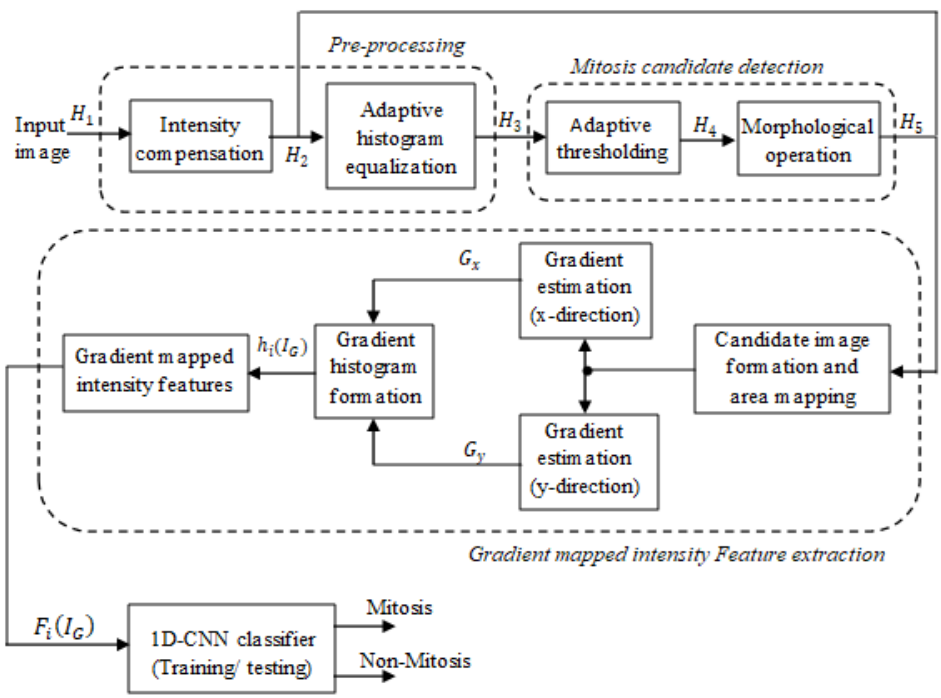

Figure 2: Block diagram representation of the proposed mitosis detection algorithm.

2.1 *Pre-processing*

Let $H_1(x,y,z)$ be the histopathological input image. Initially, the image $H_1(x,y,z)$ is applied for the intensity compensation process, which minimizes the variation in mitosis candidate detection for the images acquired from different scan instruments. The intensity compensation approach uses a compensation threshold intensity for the red, green, and blue channels. Let T_r, T_g and T_b represent the compensation threshold for the red, green, and blue channels, respectively, which can be estimated from the mean intensity of the red, green,

and blue channels of different scan images from the different datasets. Let the size of the input image $H_1(x,y,z)$ be S_1 S_2. The intensity-compensated image $H_2(x,y,z)$ can be estimated from the relation in Equation (1).

$$H_2(x,y,j) = H_1(x,y,j) + \frac{1}{S_1 \times S_2} H_1(x,y,j) - T_j \quad (1)$$

Where j∈r,g,b. The image $H_2(x,y,z)$ is applied to adaptive histogram equalization [22], which further improves the contrast of the image from which mitosis candidates are detected. Let the pre-processed image be $H_3(x,y,z)$.

2.2 *Segmentation of mitosis candidate*

For the detection of mitosis candidates, the algorithm uses adaptive thresholding [23] and morphological operations [24]. Initially, the RGB image $H_3(x,y,z)$ is converted to a grayscale image given by $H_3(x,y)$. Adaptive thresholding is then performed to obtain the image $H_4(x,y)$ that detects the possible intensities nearer to mitosis candidates. Further, the morphological operation (dilation) is performed to remove the smaller objects that do not belong to mitosis candidates. Further erosion is performed to obtain the boundaries of the mitosis candidates. Let $H_5(x,y)$ represent the image with the mitosis candidates.

2.3 *Gradient mapped intensity (GMI) feature extraction*

From the image $H_5(x,y)$, each mitosis candidate is separated to form a mitosis candidate image. The mitosis candidate image can be constructed as illustrated in Figure 3.

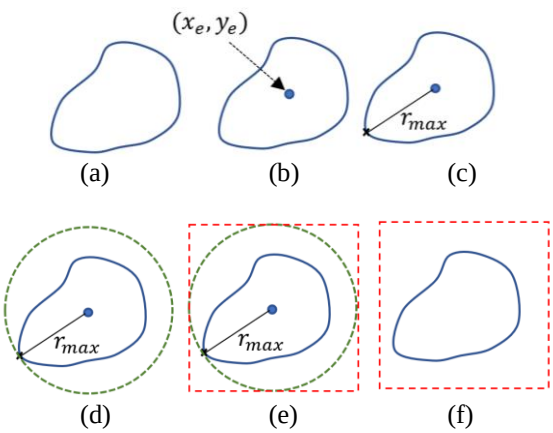

Figure 3: Estimation of mitosis candidate image (a) Mitosis candidate (b) Centroid estimation (c) Maximum radius estimation (d) Construction of circular region (e) Estimation of boundaries of mitosis candidate image (f) Representation of mitosis candidate image.

The mitosis candidate image can be reconstructed, including the processes, which are centroid estimation, maximum radius estimation, circular region construction, and boundary formation. Let $(x_1,y_1),(x_2,y_2),\ldots (x_N,y_N)$ represents the boundary pixel coordinates of a mitosis candidate shown in Figure 3(a). The centroid of the mitosis candidate (x_e, y_e) can be obtained from the boundary coordinate as shown in Figure 3(b) using the relations Equations (2) and (3).

$$(x_e, y_e) = \left(\frac{x_1, x_2, \ldots, x_N}{N}\right), \left(\frac{y_1, y_2, \ldots, y_N}{N}\right) \quad (2)$$

$$\left(x_e, y_e\right) = \left(\frac{1}{N}\sum_{n=1}^{N} x_i, \frac{1}{N}\sum_{n=1}^{N} y_i,\right) \quad (3)$$

Using the centroid x_e,y_e and the boundary pixel coordinates $(x_1,y_1),(x_2,y_2),\ldots(x_N,y_N)$, the maximum radius r_{max} is estimated as shown in Figure 3(c) using the relation Equation (4).

$$r_{max} = \max\left(\sqrt{(x_n - x_e)^2 + +(y_n - y_e)^2}\right) \quad (4)$$

where n = 1,2,…,N

Using rmax as radius and x_e, y_e as the center, a circle is constructed as shown in Figure 3(d). A square is formed such that the constructed circle is inscribed in it. Thus, the region inside the square represents the candidate image as shown in Figures 3(e) and (f).

2.3.1 Area mapping

To avoid the variation caused by to size of the mitosis candidate, the size of the mitosis candidate region is made to a uniform size A_c, which represents the number of pixels inside the mitosis candidate. Let A_c be the constant area mapping parameter. Let A_i be the area of the i^{th} mitosis candidate image. Each detected mitosis candidate image has an area of A_i that must be converted to the area of A_c. If the area of the mitosis candidate image A_i is less than the constant area mapping parameter ($A_i < A_c$), then image interpolation is performed such that $A_i \approx A_c$ as provided in Figure

4(b). The interpolation or resizing of the mitosis candidate image region is done with the scaling factor.

Similarly, if the area of the mitosis candidate image A_i is greater than the constant area mapping parameter ($A_i < A_c$), then image decimation is performed such that $A_i \approx A_c$ as provided in Figure 4(a).

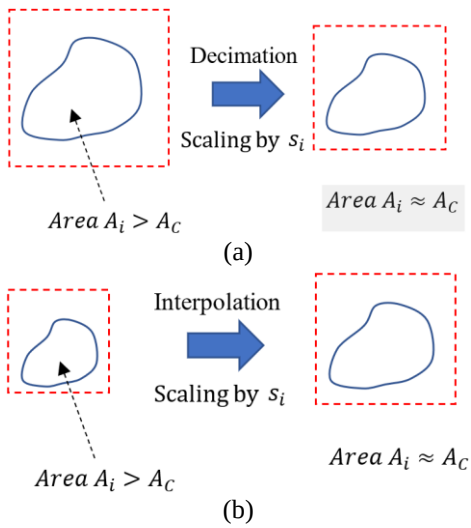

Figure 4: Area mapping for larger and smaller size mitosis candidates (a) large size mitosis candidate, (b) Small-size mitosis candidate.

The decimation or resizing of the mitosis candidate image region is done using the scaling factor s_i provided in Equation (5).

$$s_i = \frac{A_c}{A_i} \tag{5}$$

2.3.2 Gradient estimation in x and y direction

Let $H_5(x, y, z)$ represent a mitosis candidate image. From the mitosis candidate image $H_5(x, y, z)$ the gradient is estimated in x and y directions. Let (r_i, g_i, b_i) represent the red, green, and blue components of the mitosis candidate image $H_5(x, y, z)$. From each channel $r_i(x,y)$,$g_i(x,y)$ and $b_i(x,y)$, the gradient is estimated in the x and y direction. Therefore, the gradient in the x direction of red, green, and blue channels is given by $G_{xr,i}(x,y)$, $G_{xg,i}(x,y)$, and $G_{xb,i}(x,y)$, respectively. Similarly, the gradient in the direction of red, green, and blue channels is given by $G_{yr,i}(x,y)$, $G_{yg,i}(x,y)$, and $G_{yb,i}(x,y)$, respectively.

2.3.3 Gradient histogram estimation

Here, the gradient histogram $h(I_g)$, represents the number of elements with gradient values I_g. Let Δ represent the histogram spacing factor. For example, if $\Delta = 5$, it means that each bin of the histogram corresponds to five gradient values other than 0 and left and right extrema bins. From the gradient image $G_{xr,i}(x,y)$, $G_{xg,i}(x,y)$, $G_{xb,i}(x,y)$, $G_{yr,i}(x,y)$, $G_{yg,i}(x,y)$, $G_{yb,i}(x,y)$, the histogram gradient is estimated which is given by $h_{xr,i}(I_G)$, $h_{xg,i}(I_G)$, $h_{xb,i}(I_G)$, $h_{yr,i}(I_G)$, $h_{yg,i}(I_G)$, $h_{yb,i}(I_G)$, respectively (Figure 5). Here, I_G represents the intensity corresponding to the histogram bin. The histogram spacing factor $\Delta = 1$, where the histogram is estimated for each gradient value. The histogram bin for the left and right extrema is given by, $I_G \leq L_m$ *and* $I_G \geq L_M$, respectively.

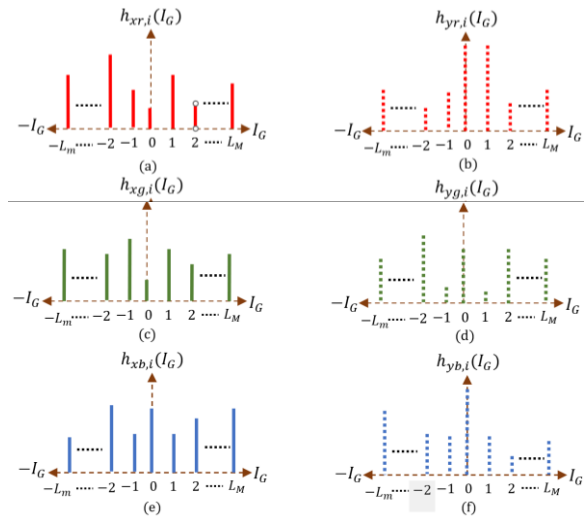

Figure 5: Representation of gradient histogram with (a) red channel in direction (b) red channel in direction (c) Green channel in direction (d) Green channel in direction (e) Blue channel in direction (f) Blue channel in direction.

For $\Delta = 1$, the intensity corresponds to the histogram is given by $I_G = \{I_G \leq L_{m,} \dots, -3, -2, -1,0,1,2,3..I_G \geq L_M\}$. For $\Delta = 5$, the intensity corresponding to the histogram is given by $I_G\{I_G \leq L_{m,..} - 15, -10, -5,0,5,10,15..I_G \geq L_M\}$. The general expression for the intensity that corresponds to the histogram with the histogram spacing factorΔ is given. $I_G = \{I_G \leq L_m, .., .., -2\Delta \leq I_G \leq -\Delta - 1, -\Delta \leq I_G \leq -1,0,1 \leq I_G \leq \Delta, \Delta + 1 \leq I_G \leq 2\Delta, .I_G \geq L_M\}$. The general structure of the gradient histogram is provided

in Figure 6(a). Figure 6(b) and (c) show the histogram representation with Δ = 1 and Δ = 5, respectively.

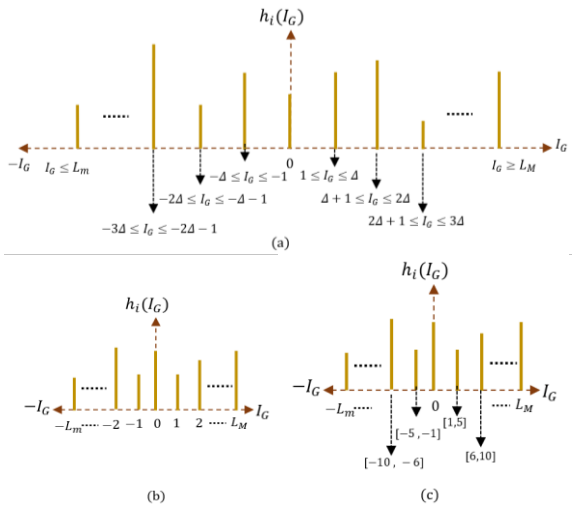

Figure 6: Representation of gradient histogram (a) General representation (b) With Δ = 1 and (c) With Δ = 5.

The histogram of the gradient values is arranged in *x*-direction R, G, and B histogram values followed by *y*-direction R, G, and B histogram values. Therefore, the features obtained by the histogram of the gradient values are expressed as Equation (6),

$$h_i(I_G) = \frac{1}{S_1 \times S_2}[h_{xr,i}(I_G), h_{xg,i}(I_G), h_{xb,i}(I_G), h_{yr,i}(I_G), h_{yg,i}(I_G), h_{yb,i}(I_G)] \quad (6)$$

The histogram of the gradient values $h_i(I_G)$ can be plotted as depicted in Figure 7(a). Let $(u_{xr,i}, v_{xr,i})$ represents the location of the gradient value I_G in the gradient image $G_{xr,i}$. The intensity feature for the gradient of the R-channel in the x-direction is estimated as Equation (7)

$$P_{xr,i}(I_G) = Mo\left(H_1(u_{xr,i}, v_{xr,i})\right)/255 \quad (7)$$

Where $Mo(.)$ is the statistical mode function. Similarly, the intensity feature for the gradient of the G and B channels in the -direction, R, G, and B channels in the -direction is estimated. The intensity feature for the mitosis candidate is expressed as Equation (8).

$$p_i(I_G) = [p_{xr,i}(I_G), p_{xg,i}(I_G), p_{xb,i}(I_G), p_{yr,i}(I_G), p_{yg,i}(I_G), p_{yb,i}(I_G)] \quad (8)$$

The intensity feature of a mitosis candidate can be plotted as shown in Figure 7(b). The histogram-mapped intensity feature for the mitosis candidate is expressed as Equation (9).

$$F_i(I_G) = [h_i(I_G), p_{xr,i}(I_G)] \quad (9)$$

The histogram-mapped gradient feature can be plotted as shown in Figure 7(c).

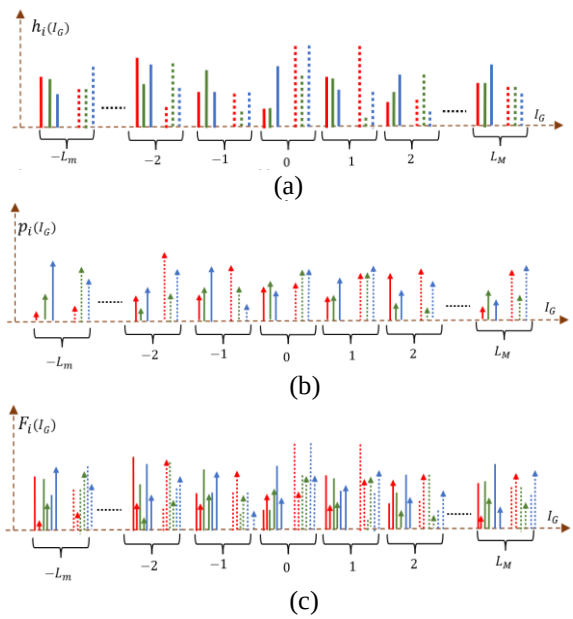

Figure 7: Representation of feature sequence (a) histogram of gradient features (b) intensity feature and (c) histogram mapped intensity feature.

2.4 *1-D-Convolutional neural network*

The result of the GMI feature extraction is one one-dimensional feature sequence. Hence, the decision to use 1D-CNN going forward. Similar to the 2-D-CNN algorithm [25], the 1-D-CNN algorithm uses four different layers, including the convolution layer, pooling layer, flatten layer, and fully connected layer (Figure 8). The convolution layer consists of different kernels or filters that perform the convolution operation between the input sequence and the filter. The max-pooling layer estimates the maximum value from the patch of the convolution output. Let *L* be the length of the feature extracted from one mitosis candidate. Therefore, the size of the convolution layer 1 and the pooling layer 1 is *L* × 32 and *L/2* × 32,

respectively. The size of the convolution layer 2 and the pooling layer 2 has the size of $L/2 \times 64$ and $L/4 \times 64$, respectively. The output of the pooling layer 2 is then flattened, which has $16L$ feature values. The fully connected layer has three sub-layers, including the input layer, hidden layers, and output layers. The input layer has $16L$ inputs, and two output layers that represent the mitosis and non-mitosis classes. The architecture uses three hidden layers in the fully connected layer, where each layer has $16L + 1$ neurons.

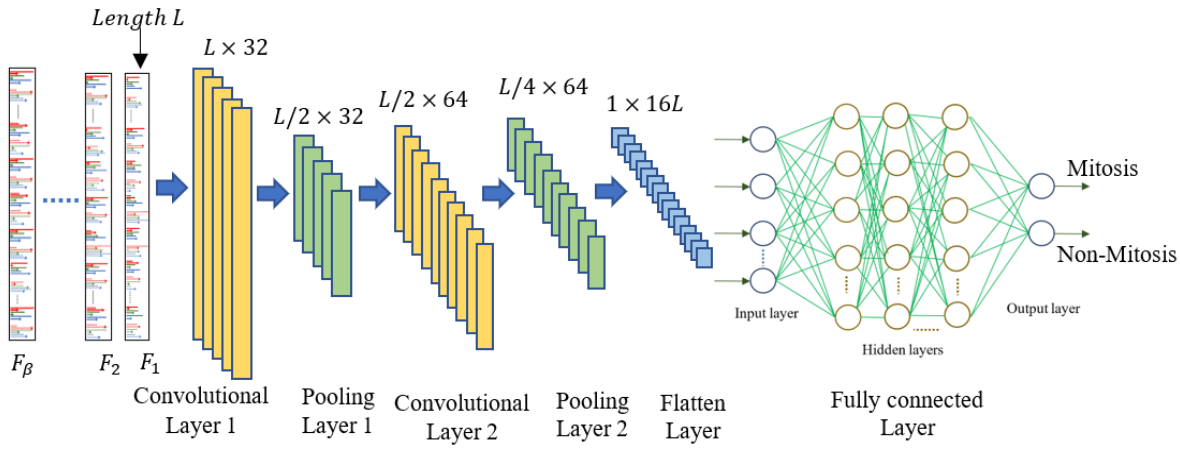

Figure 8: Architecture of 1-D-CNN for the classification of mitosis.

2.5 *Algorithm*

Input: Histopathological input scan image H_1, spacing factor Δ, left extrema L_m, right extrema L_M, Compensation thresholds of red, green, and blue channels $T_r, T_g, and\ T_b$ and respectively.

Output: Detected mitosis

Step 1: Apply Intensity compensation to the image $H_1(x,y,z)$ to obtain the intensity-compensated image $H_2(x,y,z)$.

Step 2: Perform adaptive histogram equalization on the image $H_2(x,y,z)$ to obtain the enhanced image $H_3(x,y,z)$.

Step 3: Apply adaptive thresholding to obtain the possible mitosis candidate. Let the segmented image be represented as $H_4(x,y,z)$.

Step 4: Apply the morphological operation dilation to eliminate the smaller objects that are not mitosis candidates. Further, perform erosion to obtain the boundaries of the selected mitosis candidates. Let the image that corresponds to the segmented mitosis candidate be $H_5(x,y,z)$.

Step 5: Estimate the gradients in x and y directions for the red green and blue channels of each mitosis candidate after forming a mitosis candidate image with constant area mapping.

Step 6: Estimate the gradient histogram with the spacing factor Δ, left extrema L_m, right extrema L_M. Also, estimate the gradient histogram feature.

Step 7: Estimate the intensity features using the gradient histogram and the image $H_1(x,y,z)$.

Step 8: Merge the feature obtained in steps 6 and 7 to estimate the gradient-mapped intensity features.

Step 9: Repeat steps 5 to 8 for all mitosis candidate images to obtain the complete feature $\hat{F}$.

Step 10: Train the features obtained in Step 9 with labels of the mitosis candidates using the 1-D-CNN classifier.

Step 11: Test the feature of the test image using the trained 1-D-CNN model to detect the mitosis candidates.

3 Results and Discussion

The evaluation of the mitosis detection algorithm was done using the ICPR 2012 [26] and ICPR 2014 [27] datasets with the metrics, including F1-score, recall, and precision. The sample images from the ICPR-2012 and ICPR-2014 datasets are provided in Figure 9. The images used in the ICPR 2012 dataset were acquired by an Apero-XT scanner that has a resolution of 0.2456 μm^2, which has a size of 2084×2084 pixels. The dataset has 50 images, where 15 images are used as the test images and the remaining 35 images are

used as training images. The ICPR 2014 dataset has a total of 326 labeled mitosis candidates. The ICPR 2014 dataset has 86 images, each having a size of 4000×3000. Out of 86 images, 20 images are used as test images and 66 images are used as training images. The ICPR 2014 dataset has a total of 749 labeled mitosis candidates.

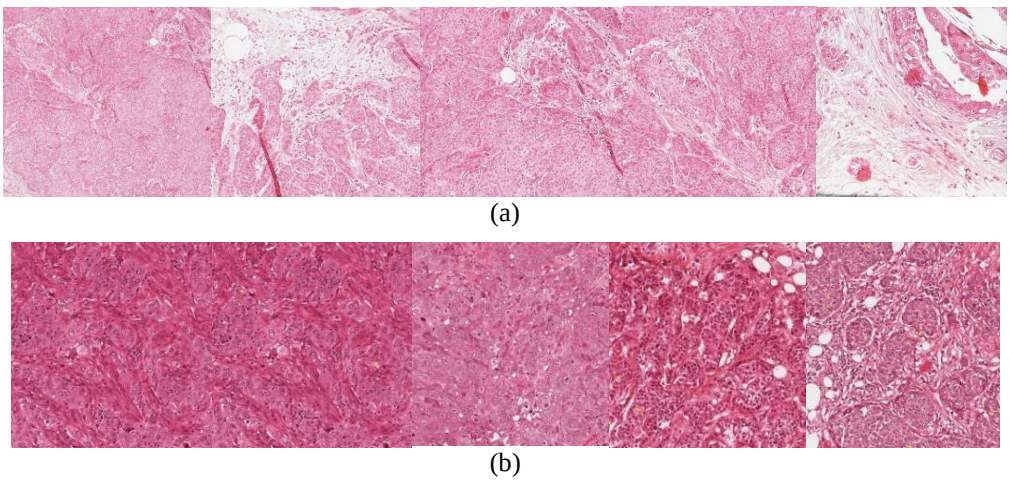

Figure 9: Sample histopathological images from ICPR-2012 and ICPR 2014 dataset (a) ICPR-2012 dataset (b) ICPR-2014 dataset.

The evaluation metrics F1-score, recall, and precision are estimated using the relation shown below Equations (10)–(12).

$$F1 - score = \frac{precision \times recall}{precision + recall} \quad (10)$$

$$Recall = \frac{T_p}{T_p + F_n} \quad (11)$$

$$precision = \frac{T_p}{T_p + F_p} \quad (12)$$

Here, F_n, T_p and F_p represent the false negative, true positive, and false positive, while classifying the mitosis candidates, respectively.

Figure 10 depicts the experimental results for the proposed mitosis candidate detection algorithm that includes the pre-processed image, mitosis candidate image, and detected mitosis. The proposed algorithm was evaluated with 11 histogram bins, including the zero-gradient intensity, left and right extrema. Thus, the total number of features extracted from one mitosis candidate is L=132. Therefore, the layer sizes of the convolution layer 1, pooling layer, convolution layer 2, and pooling layer 2 are 132 × 32, 66 × 32, 66 × 64, and respectively. The flattened and input layer of the fully connected layer has the size of 1 × 2112. We have used three hidden layers, each having 2113 neurons. The algorithm uses the red, green, and blue channel thresholds for compensation T_r, T_b, and T_g, as 136, 119, and 127, respectively. The algorithm also uses a constant area map size of 40 × 40.

Figure 11 shows a few classified mitosis candidates. The performance of the proposed scheme is compared with the traditional approaches, including HC+CNN [28], IPAL [29], CasNN [17], IDSIA [16], RRF [30], DeepMitosis [2], Condinst [31], SegMitosis [32], CDAM [6], and Boxinst [33]. The proposed approach provides an F1-score of 0.846, which is 1.4% higher than SegMitosis approach for ICPR 2012 dataset (Table 1). The precision of the proposed approach is 0.9% and 2.4% higher than the SegMitosis and Boxinst scheme for ICPR 2012 and ICPR 2014 dataset, respectively (Figure 12). Hence, proving that the proposed method has better accuracy when working with the datasets.

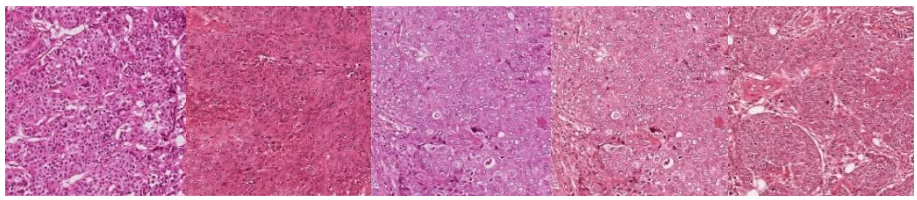

(a)

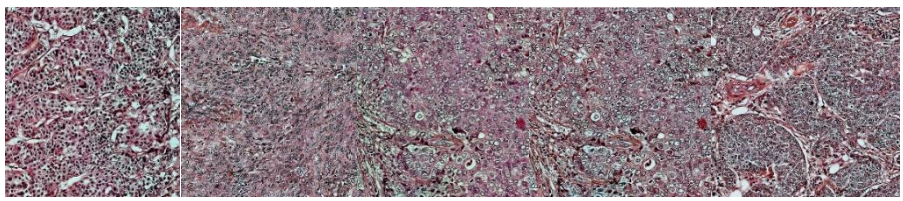

(b)

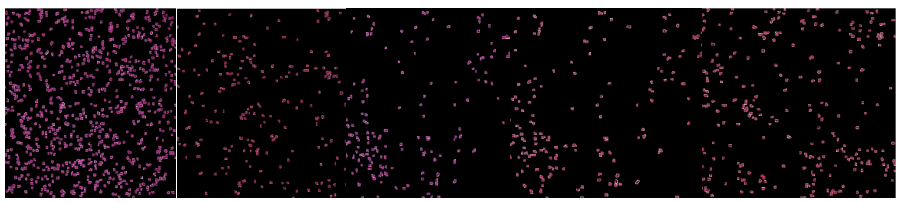

(c)

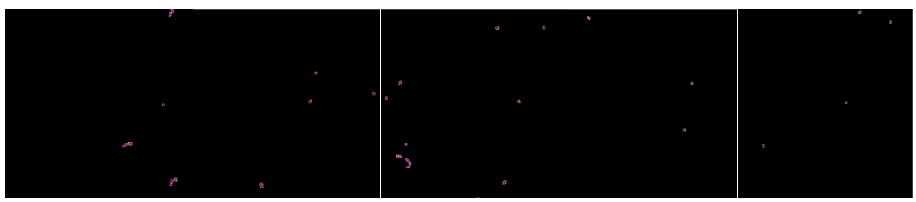

(d)

Figure 10: Experimental results for mitosis candidate detection (a) Input image (b) Pre-processed image (c) Mitosis candidates, (d) Detected mitosis.

(a)

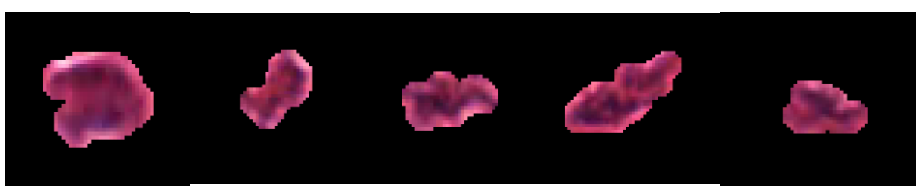

(b)

Figure 11: Few of the mitosis candidate results for mitosis and non-mitosis cells (a) Mitosis cells (b) non-mitosis cells.

Table 1: Performance comparison of the proposed approach with the traditional approach for ICPR 2012 and ICPR 2014 dataset.

Method	ICPR 2012			ICPR 2014		
	F1-score	Recall	Precision	F1-score	Recall	Precision
HC+CNN	0.735	0.65	0.84	0.521	0.462	0.472
IPAL	0.718	0.74	0.698	0.538	0.473	0.487
CasNN	0.788	0.772	0.804	0.557	0.496	0.463
IDSIA	0.782	0.7	0.88	0.569	0.567	0.473
RRF	0.823	0.811	0.835	0.582	0.583	0.485
Deep Mitosis	0.802	0.762	0.846	0.572	0.621	0.488
Condinst	0.830	0.832	0.832	0.612	0.653	0.521
SegMitosis	0.832	0.812	0.854	0.607	0.785	0.495
CDAM	0.825	0.842	0.81	0.631	0.691	0.581
Boxinst	0.812	0.792	0.833	0.629	0.689	0.593
Proposed	0.846	0.859	0.863	0.659	0.763	0.617

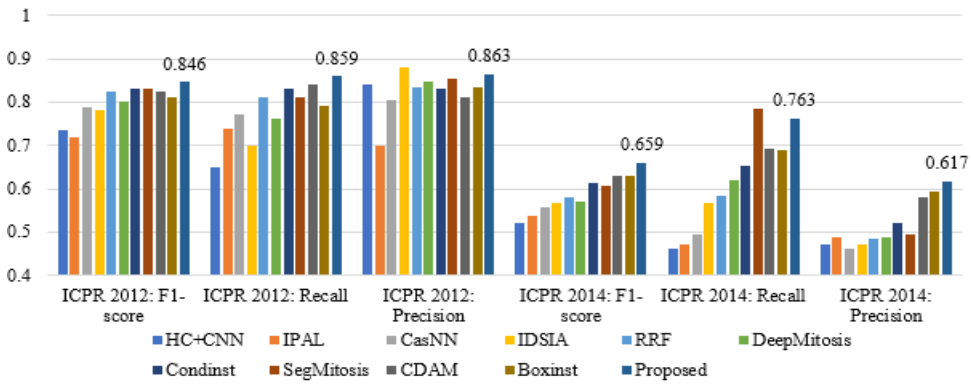

Figure 12: Graphical comparison of the performance of the proposed approach with traditional schemes.

Table 2: k-fold validation results for ICPR 2012 and ICPR 2014 datasets.

Fold	ICPR 2012			ICPR 2014		
	F1-score	Recall	Precision	F1-score	Recall	Precision
1	0.832	0.814	0.871	0.662	0.759	0.61
2	0.862	0.863	0.876	0.631	0.771	0.629
3	0.857	0.849	0.833	0.653	0.757	0.631
4	0.821	0.872	0.867	0.662	0.751	0.609
5	0.858	0.897	0.868	0.687	0.777	0.595
Avg	0.846	0.859	0.863	0.659	0.763	0.617

The validation of the algorithm was performed using the k-fold cross-validation with k = 1, 2, 3, 4, and 5. It helps assess the results of the model and generalize to an independent dataset. Also, ensuring that the model's evaluation is less biased and better represents how the model would perform on an unseen dataset. The results obtained using the k-fold cross-validation for different values of k are illustrated in Table 2. The average F1-score, recall, and precision for the proposed approach for the ICPR 2012 dataset are estimated as 0.846, 0.859, and 0.863, respectively. For the ICPR 2014 dataset, the F1-score, recall, and precision were estimated as 0.659, 0.763, and 0.617, respectively.

With the left and right extrema L_m = -22 and L_m = 22, the number of histogram bins and feature-length can be estimated as illustrated in Table 3. As the spacing factor increases, the feature length reduces.

Table 3: Estimation of feature length for different spacing factor.

Spacing Factor Δ	#Histogram Bins	Feature Length
1	45	540
3	17	204
5	11	132
7	9	108
9	7	84

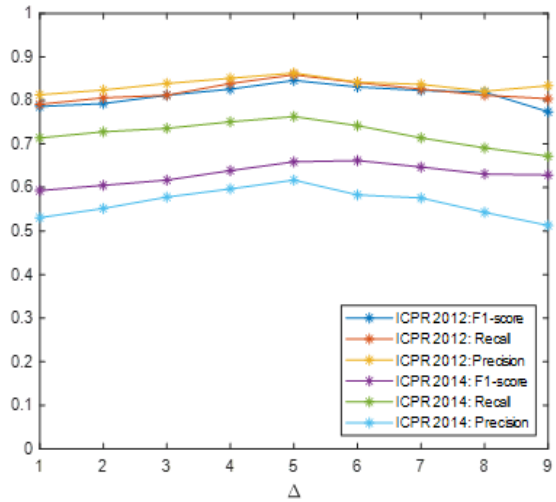

Figure 13: Performance variation for different values of Δ.

Figure 13 shows the graphical representation of the variation of performance metrics F1-score, recall, and precision for different values of the spacing factor Δ. As the spacing factor Δ is increased from 1, the performance gradually increases. The maximum performance can be obtained for the spacing factor Δ = 5. As the spacing factor is further increased, the performance gradually reduces.

Table 4 shows the training and testing time comparison for different values of Δ. The training and testing time of ICPR-2014 is higher than the ICPR-2012 dataset. For Δ = 5, the training time of the ICPR-2012 and ICPR-2014 datasets is 1859.16s and 2318.97s, respectively. Similarly, for Δ = 5, the testing time of the ICPR-2012 and ICPR-2014 datasets is 0.861s and 0.976, respectively. The graphical comparison of training and testing time complexity is provided in Figure 14. As the value of Δ increases, the training and testing time is reduced. This is due to the reduction in the number of features extracted from each mitosis candidate. The reduction in features reduces the training and classification time of the CNN network.

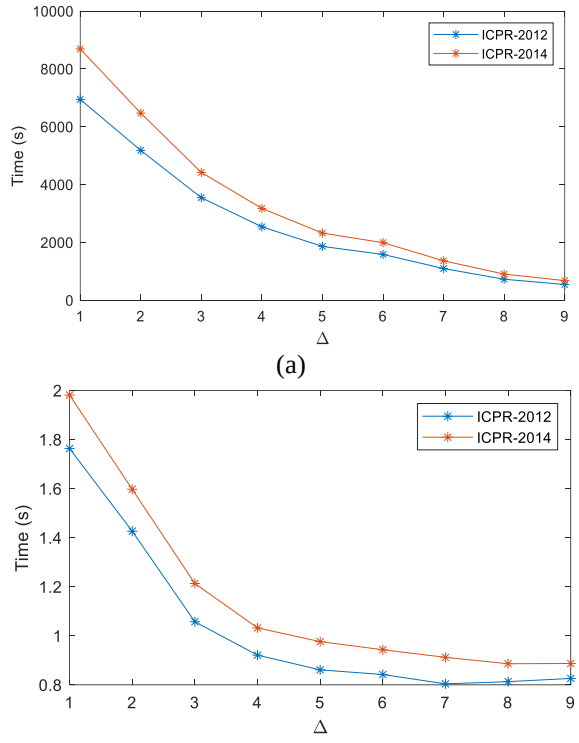

Figure 14: Comparison of training and testing time for different values of Δ (a) Training time (b) testing time.

Table 4: Time complexity comparison for different values of spacing factor.

		1	2	3	4	5	6	7	8	9
ICPR -2012	**Train**	6943.41	5179.33	3543.81	2536.09	1859.16	1581.13	1094.592	723.344	542.504
	Test	8689.32	6469.17	4417.35	3172.61	2318.97	1989.46	1361.36	901.21	676.17
ICPR -2014	**Train**	1.763	1.426	1.057	0.921	0.861	0.842	0.804	0.813	0.826
	Test	1.981	1.597	1.213	1.032	0.976	0.943	0.912	0.886	0.887

4 Conclusions

The paper proposed a mitosis detection algorithm on histopathological images that extracts gradient-mapped intensity features. The algorithm uses a 1-D CNN for the classification of one-dimensional vector GMI features extracted from the mitosis candidates. The scheme uses four processes, including pre-processing, mitosis candidate detection, GMI feature extraction from the candidates, and 1-D CNN classification. After pre-processing the histopathological images, the mitosis candidates are detected using adaptive thresholding and morphological operations, which are dilation and erosion. From the mitosis candidate, GMI features are extracted that include the stages like gradient estimation in *x*, and *y* direction, formation of gradient histogram, and mapping of gradient and intensity

components. Finally, the extracted GMI features from each mitosis candidate are trained and classified using a 1-D CNN classifier. The evaluation of the 1-D CNN classifier with GMI features is evaluated with performance metrics such as F1-score, recall, and precision. The proposed scheme provides the F1-score, recall, and precision of 0.846, 0.859, and 0.863, respectively, for the ICPR 2012 dataset. From the evaluation results, the proposed approach outperforms other similar approaches when evaluated in the ICPR 2012 and ICPR 2014 datasets.

As an extension of the work, the algorithm can be extended to other forms of cancer histopathological image analysis. The algorithm helps to build similar models that can classify the mitotic and non-mitotic cells, where they can be from images from different microscopes, different datasets, etc. This detection algorithm can be further improved by incorporating domain adoption and stain normalization techniques. Thereby improving the model's robustness and generalizability across histopathological images from different equipment and labs.

Author Contributions

A.J: conceptualization, investigation, reviewing and editing; A.J.: investigation, methodology, writing an original draft; A.J, D.V.C.: research design, data analysis; A.J, P.W, J.T.: conceptualization, data curation, writing—reviewing and editing. All authors have read and agreed to the published version of the manuscript.

Conflicts of Interest

The authors declare no conflict of interest.

References

[1] C. W. Elston and I. O. Ellis, "Pathological prognostic factors in breast cancer. I. The value of histological grade in breast cancer: Experience from a large study with long-term follow-up," *Histopathology*, vol. 19, no. 5, pp. 403–410, 1991.

[2] C. Li, X. Wang, W. Liu, and L. J. Latecki, "DeepMitosis: Mitosis detection via deep detection, verification and segmentation networks," *Medical Image Analysis*, vol. 45, pp. 121–133, Apr. 2018.

[3] H. Chen, Q. Dou, X. Wang, J. Qin, and P. A. Heng, "Mitosis detection in breast cancer histology images via deep cascaded networks," in *Proceedings of the AAAI Conference on Artificial Intelligence*, 2016, pp. 1160–1166.

[4] D. C. Cireșan, A. Giusti, L. M. Gambardella, and J. Schmidhuber, "Mitosis detection in breast cancer histology images with deep neural networks," in *International Conference on Medical Image Computing and Computer-Assisted Intervention*, 2013, pp. 411–418.

[5] H. Lei, S. Liu, A. Elazab, X. Gong, and B. Lei, "Attention-guided multi-branch convolutional neural network for mitosis detection from histopathological images," *IEEE Journal of Biomedical and Health Informatics (JBHI)*, vol. 25, no. 2, pp. 358–370, 2020.

[6] Y. Li, Y. Xue, L. Li, X. Zhang, and X. Qian, "Domain adaptive box-supervised instance segmentation network for mitosis detection," *IEEE Transactions on Medical Imaging*, 2022.

[7] N. Inoue, R. Furuta, T. Yamasaki, and K. Aizawa, "Cross-domain weakly-supervised object detection through progressive domain adaptation," in *the IEEE/CVF Conference on Computer Vision and Pattern Recognition*, Jun. 2018, pp. 5001–5009.

[8] Y. Chen, W. Li, C. Sakaridis, D. Dai, and L. Van Gool, "Domain adaptive faster R-CNN for object detection in the wild," in *Proc. IEEE/CVF Conf. Comput. Vis. Pattern Recognit.*, Jun. 2018, pp. 3339–3348.

[9] M. Suchetha, N. S. Ganesh, R. Raman, and D. E. Dhas, "Region of interest-based predictive algorithm for subretinal hemorrhage detection using faster R-CNN," *Soft Computing*, vol. 25, no. 24, pp. 15255–15268, 2021.

[10] Y. Xue, G. Bigras, J. Hugh, and N. Ray, "Training convolutional neural networks and compressed sensing end-to-end for microscopy cell detection," *IEEE Transactions on Medical Imaging*, vol. 38, no. 11, pp. 2632–2641, Nov. 2019.

[11] X. Zhao, S. Liang, and Y. Wei, "Pseudo mask augmented object detection," in *the IEEE/CVF Conference on Computer Vision and Pattern Recognition*, Jun. 2018, pp. 4061–4070.

[12] D. Tellez, M. Balkenhol, I. Otte-Höller, R. van de Loo, R. Vogels, and P. Bult, "Whole-slide mitosis detection in H&E breast histology using PHH3 as a reference to train distilled stain-

invariant convolutional networks," *IEEE Transactions on Medical Imaging*, vol. 37, no. 9, pp. 2126–2136, Sep. 2018.

[13] Y. Zhang, H. Chen, Y. Wei, P. Zhao, J. Cao, X. Fan, X. Lou, H. Liu, J. Hou, X. Han, J. Yao, Q. Wu, M. Tan, and J. Huang, "From whole slide imaging to microscopy: Deep microscopy adaptation network for histopathology cancer image classification," in *International Conference on Medical Image Computing and Computer-Assisted Intervention*, 2019, pp. 360–368.

[14] C. Huang and H. Lee, "Automated mitosis detection based on exclusive independent component analysis," in *Proceedings of the 21st International Conference on Pattern Recognition (ICPR2012)*, 2012, pp. 1856–1859.

[15] A. M. Khan, H. El-Daly, and N. M. Rajpoot, "A gamma-gaussian mixture model for detection of mitotic cells in breast cancer histopathology images," in *Proceedings of the 21st International Conference on Pattern Recognition (ICPR2012)*, 2012, pp. 149–152.

[16] D. C. Cireşan, A. Giusti, L. M. Gambardella, and J. Schmidhuber, "Mitosis detection in breast cancer histology images with deep neural networks," in *International Conference on Medical Image Computing and Computer-Assisted Intervention*, 2013, pp. 411–418.

[17] H. Chen, Q. Dou, X. Wang, J. Qin, and P. A. Heng, "Mitosis detection in breast cancer histology images via deep cascaded networks," in *Proceedings of the Thirtieth AAAI Conference on Artificial Intelligence*, 2016, pp. 1160–1166.

[18] H. Wang, A. Cruz-Roa, A. Basavanhally, H. Gilmore, N. Shih, M. Feldman, J. Tomaszewski, F. Gonzalez, A. Madabhushi, "Mitosis detection in breast cancer pathology images by combining handcrafted and convolutional neural network features," *Journal of Medical Imaging*, vol. 1, 2014, Art. no. 034003.

[19] S. Ren, K. He, R. Girshick, and J. Sun, "Faster R-CNN: Towards real-time object detection with region proposal networks," in *Advances in Neural Information Processing Systems (NeurIPS)*, 2015, pp. 91–99.

[20] J. Hu, L. Shen, S. Albanie, G. Sun, and E. Wu, "Squeeze-and-excitation networks," in *IEEE Conference on Computer Vision and Pattern Recognition (CVPR)*, 2018, pp. 7132–7141.

[21] M. Al-Imran, A. C. Das, M. A. Hasan, M. N. H. Mir, M. J. Ahmmed, T. Rahman, R. J. Bhuiyan, M. A. S. Mozumder, S. Akter, and M. E. Hossen, "Evaluating machine learning algorithms for breast cancer detection: A study on accurecy and predictive performance," *The American Journal of Engineering and Technology*, vol. 6, pp. 22–33, 2024.

[22] S. M. Pizer, E. P. Amburn, J. D. Austin, R. Cromartie, A. Geselowitz, T. Greer, B. ter Haar Romeny, J. B. Zimmerman, and K. Zuiderveld, "Adaptive histogram equalization and its variations," *Computer Vision, Graphics, and Image Processing*, vol. 39, no. 3, pp. 355–368, 1987.

[23] P. Roy, S. Dutta, N. Dey, G. Dey, S. Chakraborty, and R. Ray, "Adaptive thresholding: A comparative study," in *International Conference on Intelligent Computing, Instrumentation and Control Technologies (ICICICT)*, 2014, pp. 1182–1186.

[24] M. L. Comer and E. J. Delp III, "Morphological operations for color image processing," *Journal of Electronic Imaging*, vol. 8, no. 3, pp. 279–289, 1999.

[25] S. Das, K. Kharbanda, M. Suchetha, R. Raman, and D. E. Dhas, "Deep learning architecture based on segmented fundus image features for classification of diabetic retinopathy," *Biomedical Signal Processing and Control*, vol. 68, 2021, Art. no. 102600.

[26] C. Huang and H. Lee, "Automated mitosis detection based on exclusive independent component analysis," in *Proceedings of the 21st International Conference on Pattern Recognition (ICPR2012)*, 2012, pp. 1856–1859.

[27] ICPR. "ICPR 2014 Mitosis Detection Dataset." mitos-atypia-14.grand-challenge.org. https://mitos-atypia-14.grand-challenge.org/home/ (accessed Nov. 19, 2022).

[28] H. Wang, A. Cruz-Roa, A. Basavanhally, H. Gilmore, N. Shih, M. Feldman, J. Tomaszewski, F. Gonzalez, A. Madabhushi, "Cascaded ensemble of convolutional neural networks and handcrafted features for mitosis detection," in *SPIE Conference Proceedings*, 2014, vol. 9041.

[29] H. Irshad, "Automated mitosis detection in histopathology using morphological and multi-channel statistics features," *Journal of Pathology Informatics*, vol. 4, pp. 10–17, 2013.

[30] A. Paul, A. Dey, D. P. Mukherjee, J. Sivaswamy, and V. Tourani, "Regenerative random forest with automatic feature selection to detect mitosis in histopathological breast cancer images," in *International Conference on Medical Image Computing and Computer-Assisted Intervention*, 2015, pp. 94–102.

[31] Z. Tian, C. Shen, and H. Chen, "Conditional convolutions for instance segmentation," in *16th European Conference on Computer Vision (ECCV)*, 2020, pp. 282–298.

[32] C. Li, X. Wang, W. Liu, L. J. Latecki, B. Wang, and J. Huang, "Weakly supervised mitosis detection in breast histopathology images using concentric loss," *Medical Image Analysis*, vol. 53, pp. 165–178, 2019.

[33] Z. Tian, C. Shen, X. Wang, and H. Chen, "BoxInst: High-performance instance segmentation with box annotations," in *Proceedings of the IEEE conference on computer vision and pattern Recognition (CVPR)*, Jun. 2021, pp. 5443–5452.

[34] M. T. Imran, I. Shafi, J. Ahmad, M. F. U. Butt, S. G. Villar, E. G. Villena, T. Khurshaid, and I. Ashraf, "Virtual histopathology methods in medical imaging - A systematic review," *BMC Medical Imaging*, vol. 24, no. 1, p. 318, Nov. 2004.

[35] J. Wang, T. Wang, R. Han, D. Shi, and B. Chen, "Artificial intelligence in cancer pathology: Applications, challenges, and future directions," *Cytojournal*, vol. 22, p. 45, 2025.